

Local Piston Theory with Viscous Correction and Its Application

Wen Liu*

Northwestern Polytechnical University, Xi'an 710072, People's Republic of China

Chen-An Zhang†

Chinese Academy of Sciences, Beijing 100190, People's Republic of China

Han-Qiao Han‡

Wuhan Second Ship Design and Research Institute, Wuhan 430072, People's Republic of China
and

Fa-Min Wang§

Chinese Academy of Sciences, Beijing 100190, People's Republic of China

DOI: 10.2514/1.J055207

This paper introduces a local piston theory with viscous correction for the prediction of hypersonic unsteady aerodynamic loads at high attitudes and large Mach numbers. A semi-empirical relation accounting for the viscous interaction effects to determine the effective shape is proposed. The method is validated by applying to thin airfoils at various Mach numbers, angles of attack, and operating altitudes. Sample two- and three-dimensional aerodynamic forces calculations are conducted demonstrating this method. Furthermore, flutter boundary predictions for a two-dimensional airfoil and pitching-in-damping derivative evaluations for a three-dimensional waverider configuration are performed with this unsteady aerodynamic model. Compared with the Euler-based local piston theory, this model performs much better at high altitudes for a wide range of Mach numbers, angles of attack, and shapes. Results suggest the feasibility of using the effective shape of hypersonic vehicles to efficiently and accurately obtain the unsteady aerodynamic characteristics in hypersonic flow environment.

Nomenclature

a	=	dimensionless offset between the elastic axis and the midchord, positive for elastic-axis locations behind midchord
a_∞	=	speed of sound
b	=	$c/2$, airfoil semichord
C_{eff}	=	effective shape determination coefficient
C_l	=	lift coefficient
C_m	=	pitching moment coefficient
$C_m^{\omega_z}, C_m^{\dot{\alpha}}$	=	derivative of C_m with respect to ω_z and $\dot{\alpha}$
C_N	=	normal force coefficient
C_p	=	pressure coefficient
c	=	chord length, reference length
H	=	altitude
h	=	plunge displacement at the elastic axis, positive down
I_α	=	cross-sectional mass moment of inertia about its elastic axis
k	=	$\omega c/(2u_\infty)$, reduced frequency
k_c	=	$\omega c/u_\infty$, reduced frequency
L	=	sectional lift force, positive up
L_c	=	length of the generating cone
M	=	Mach number
M_{EA}	=	sectional aerodynamic moment about the elastic axis
m	=	airfoil mass per unit span

p	=	pressure
r_α	=	dimensionless radius of gyration about elastic axis
S_α	=	static moment per unit span
T	=	temperature
T_w	=	wall temperature
t	=	time
u_∞	=	freestream velocity
u, v, w	=	velocity along the X, Y , and Z axes
\bar{V}'	=	viscous interaction parameter
V_f^*	=	reduced flutter speed
W	=	downwash speed
X_{cg}	=	relative location of center of gravity along X axis
x, y, z	=	spatial coordinates
x_α	=	dimensionless static imbalance of the airfoil about its elastic axis
α	=	angle of attack, torsion deflection
α_0	=	mean angle of attack
β	=	shock-wave angle
$\delta\alpha$	=	amplitude of the pitch motion
γ	=	ratio of the specific heats
δ^*	=	displacement thickness
ξ	=	vorticity
ρ	=	density
τ	=	slope of the airfoil surface
τ_w	=	$\omega_\alpha \cdot t$, dimensionless time
τ_c	=	$t/(c/u_\infty)$, dimensionless time
φ	=	azimuth angle
ω	=	circular frequency
ω_α, ω_h	=	uncoupled frequency of plunging and pitching
ω_z	=	angular velocity around Z axis

Received 19 March 2016; revision received 28 July 2016; accepted for publication 7 August 2016; published online 24 October 2016. Copyright © 2016 by the American Institute of Aeronautics and Astronautics, Inc. All rights reserved. All requests for copying and permission to reprint should be submitted to CCC at www.copyright.com; employ the ISSN 0001-1452 (print) or 1533-385X (online) to initiate your request. See also AIAA Rights and Permissions www.aiaa.org/randp.

*Ph.D. Candidate, National Key Laboratory of Aerodynamic Design and Research; currently Visiting Student, State Key Laboratory of High Temperature Gas Dynamics, Institute of Mechanics, Chinese Academy of Sciences, Beijing 100190, PRC.

†Assistant Professor, State Key Laboratory of High Temperature Gas Dynamics, Institute of Mechanics (Corresponding Author).

‡Engineer, General Performance Group.

§Professor, State Key Laboratory of High Temperature Gas Dynamics, Institute of Mechanics.

I. Introduction

SEVERAL hypersonic flight programs have been performed to explore the design of hypersonic vehicles in the past decades, such as National Aerospace Plane, Force Application and Launch from Continental United States, VentureStar, Hypersonic International Flight Research, etc. Significant progress has been made in the hypersonic technologies, but there remains much work to do in the field of aerodynamics, control, materials, and so on. These flight vehicles operate prolonged maneuver flight at high altitudes ($H = 40\text{--}70$ km)

and high Mach numbers ($M \geq 10$). In such a flight condition, the common slender body and flexible control surfaces of the hypersonic vehicles will suffer from extreme aerodynamic heating and loading and will most likely experience structural deformations, all of which make it challenging to successfully perform aerodynamic configuration design and to accurately evaluate aerodynamic characteristics, including aeroelasticity, aerothermoelasticity, flight dynamics, etc. Currently, because of the difficulty in realizing the stable and sustained airflow simulation of high altitudes and high Mach numbers, the hypersonic wind-tunnel experiment technique is far from being mature. Thus, an alternate way for predicting hypersonic unsteady aerodynamic loads is through the use of computational fluid dynamics (CFD) [1]. In recent years, the rapid advancement in computer technologies enables the use of CFD in the modeling of unsteady aerodynamics. However, because the time-step size in unsteady CFD calculations has to decrease as the Mach number increases, using CFD approaches in hypersonic speeds will need lots of computational time and resources, which is especially unacceptable for preliminary design and trend-type research of hypersonic vehicles. To solve the preceding problems, one of the primary tasks is to model the unsteady aerodynamic forces accurately and efficiently.

Researchers have developed a number of approximate unsteady aerodynamic theories in history due to the limited capabilities of computational methods, such as Newtonian impact theory, shock-wave/expansion-wave method, piston theory, Van Dyke's second-order theory, and so on [2–5]. These methods are based on a number of assumptions including inviscid flow and simple geometries. Hence, they cannot be used in complex problems. Morgan et al. proposed the local piston theory [6], which can be used in problems of large angles of attack by replacing freestream flow quantities with local flow terms computed with the shock-wave/expansion-wave method. More recently, several approaches that combine steady inviscid CFD solutions and traditional analytical methods emerged. Scott and Pototzky proposed a quasi-steady approach, using two separate steady CFD solutions per vibratory mode: one solution for the static part and another for the harmonic part of the pressure, to obtain the generalized aerodynamic forces for flutter analysis [7]. Zhang et al. developed an Euler-based local piston theory (LPT), incorporating the solutions of steady Euler equations into the approximate method [8,9]. Such hybrid steady-state CFD/analytical approaches are appealing because the steady flow analysis can capture complex flow phenomena neglected by classical aerodynamic theories and are not limited by the shape of the objects [10], and they are much more computationally efficient than unsteady CFD analysis. However, because these methods are based on the solutions of inviscid flow, the accuracy will inevitably become poor when applied to problems at high altitudes, where the inviscid–viscous interactions have a significant effect on the aerodynamic characteristics.

McNamara et al. proposed an approach that combines the pressure calculated from the steady Navier–Stokes (N-S) equations and unsteady component of the pressure extracted from piston theory (NS_{SS-PT}) and achieved better results than LPT for the cases studied [10,11]. Meanwhile, they pointed out that the boundary layer caused by the viscosity changes the effective shape of the body, leading to the low accuracy of piston theory. Therefore, two methods were employed to calculate the boundary-layer displacement thickness, including a semi-empirical equation [12] and a method approximated from steady-state CFD flow analysis. Then, the third-order piston theory was applied on the effective shape instead of the original surface. However, this method did not show better accuracy than LPT and NS_{SS-PT}. The authors also mentioned that the difficulty in identifying the local Mach number at the edge of the boundary layer, not known a priori, limited the incorporation of inviscid–viscous interactions into the CFD-based methods.

Han et al. developed a local piston theory with viscous correction for the prediction of hypersonic unsteady aerodynamic loads at high altitudes [13]. They attempted to obtain the effective shape and identify its local flow quantities from the steady Navier–Stokes numerical solutions for the viscous correction of LPT. There, the

authors proposed a semi-empirical relation for the determination of effective shape. In this paper, we try to further improve this method by discussing the range of application and extending it from two-dimensional airfoils to three-dimensional configurations. Furthermore, this method is applied to predict the flutter boundaries and evaluate the pitching dynamic stability characteristics.

II. Computational-Fluid-Dynamics Solver

A. Numerical Method

The CFD solver GMFlow is used in the paper. A cell-centered finite volume method is employed to solve the Euler and Reynolds-averaged Navier–Stokes equations. The AUSM+ spatial discretization scheme is adopted with an implicit lower-upper symmetric Gauss-Seidel scheme for the temporal integration. The governing equations are solved using the dual-time-stepping method, and local time stepping with the fourth-order Runge–Kutta scheme is used at the subiteration. Moreover, the scheme of grid deformation is based on the Radial Basis Function interpolation [14]. For computations of viscous flows, the one-equation Spalart–Allmaras turbulence model is implemented at the altitudes $H < 40$ km, whereas the laminar flow model is used at the altitudes $H \geq 40$ km. More details about the numerical methods can be found in [15,16].

B. Solver Validation

The accuracy of the unsteady aerodynamic codes is validated in [17], where the transonic unsteady aerodynamics of the NACA 0012 airfoil calculated by GMFlow are compared with the experimental results in [18].

The success of the methodology proposed in the paper depends on the accuracy of steady N-S solutions under the condition of strong viscous interaction. Therefore, an example of the orbital vehicle OV-102 is conducted to verify the reliability of the numerical methods. The following flight condition is given in [19]: $M = 20$, angle of attack (AOA) = 20 deg, $\gamma = 1.15$, $T_w = 1366$ K, and $H = 40, 50, 60, 70, 75$ km. The wall mesh of OV-102 is shown in Fig. 1, and the lift-to-drag ratio (L/D) at different conditions is shown in Fig. 2. The results calculated from the current numerical methods are quite close to those from [19], showing that the CFD solver is reliable in the application of problems under the condition of strong viscous interaction.

III. Local Piston Theory

A. Derivation of Local Piston Theory

The classical piston theory assumes that perturbations spread along the normal direction to the surface for $M \gg 1$, as if caused by the action of a piston. Using the momentum equation and the isentropic assumption, one obtains the following basic piston theory formula for the surface pressure:

$$p = p_\infty \left(1 + \frac{\gamma - 1}{2} \frac{W}{a_\infty} \right)^{(2\gamma/\gamma-1)} \quad (1)$$

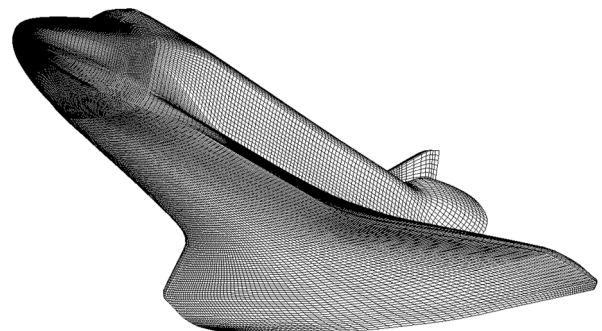


Fig. 1 Mesh of OV-102.

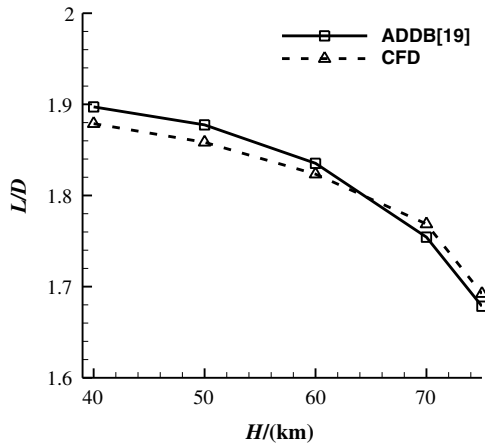


Fig. 2 Comparison of L/D at different altitudes.

where W is the downwash speed, p_∞ is the pressure of freestream, a_∞ is the sound speed of the freestream, and γ is the ratio of the specific heats. Equation (1) is a seventh-order formula about W when $\gamma = 1.4$. In the condition of small perturbations [$M(W/a_\infty) \ll 1$], we may use the linearized first-order formula:

$$C_p = \frac{2}{M^2} \left(\frac{W}{a_\infty} \right) \quad (2)$$

or the second-order formula:

$$C_p = \frac{2}{M^2} \left[\frac{W}{a_\infty} + \frac{\gamma + 1}{4} \left(\frac{W}{a_\infty} \right)^2 \right] \quad (3)$$

It should be noticed that the classical piston theory is based on the assumption of small perturbation relative to the freestream. As such, it can only be used in the problems of thin airfoils at small angles of attack.

To remove the limitations, local piston theory replaces the freestream quantities with the local flow terms, so that it realizes unsteady prediction based on steady flow. By applying Eq. (1) locally and keeping only the first-order terms, Zhang et al. [9] gives the following Euler-based local piston theory:

$$\begin{cases} P = P_l + \rho_l a_l W \\ W = \mathbf{V}_l \cdot \delta \mathbf{n} + \mathbf{V}_b \cdot \mathbf{n} \\ \delta \mathbf{n} = \mathbf{n}_0 - \mathbf{n} \end{cases} \quad (4)$$

where \mathbf{n}_0 is the outward normal unit vector before deformation; \mathbf{n} is the outward normal unit vector after deformation; W is the local downwash speed due to both deformation $\mathbf{V}_l \cdot \delta \mathbf{n}$ and vibration $\mathbf{V}_b \cdot \mathbf{n}$; and P_l , ρ_l , a_l , and \mathbf{V}_l are the local pressure, density, sound speed, and flow velocity, respectively. All the local flow quantities are computed by the steady Euler solver.

B. Range of Application of Local Piston Theory

Compared with the classical piston theory, LPT accounts for the nonlinear effects of the steady flow through accurately capturing the local flow quantities. In terms of computational efforts, only one steady Euler solution is needed for each flight condition. Results in [9,20] show that this method not only removes the limitations of classical piston theory on the airfoil thickness, angles of attack, and

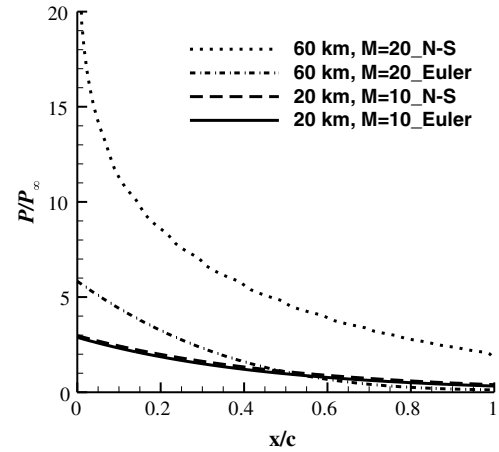


Fig. 3 Dimensionless pressure for the 4% circular-arc airfoil.

flight Mach numbers but also yields reasonable accuracy for airfoils with round leading edges in supersonic flow, mainly because the large perturbations and nonlinearity are accounted for by the steady Euler solver.

However, LPT is based on the assumption of inviscid flow. In a real flight with the speed of $M > 10$, the flight vehicle is supposed to fly at a relatively high altitude ($H = 40\text{--}70$ km), where the Reynolds number may be on the order of $10^5\text{--}10^6$. The dimensionless wall pressure distribution of a 4% thickness circular-arc airfoil is plotted in Fig. 3, under the condition of $H = 20$ km, $M = 10$ and $H = 60$ km, $M = 20$, respectively, from the steady-state CFD solutions at zero angle of attack (AOA). At 20 km, the wall pressure from inviscid and viscous results is almost coincident, whereas at 60 km, the pressure from the N-S results is apparently larger than that from the Euler results. Such a phenomenon can be explained by the viscous interaction effect. Under some conditions of high altitudes and high Mach numbers, the very large boundary-layer thickness displaces the outer inviscid flow, changing the nature of the inviscid flow. In turn, the substantial changes in the outer inviscid flow feed back to the boundary layer, affecting its growth and properties. The mutual interaction process between the boundary layer and the outer inviscid flow is called viscous interaction [2]. Obviously, under the condition of $H = 20$ km, $M = 10$, the viscous interaction is not strong enough to change the inviscid wall pressure distribution significantly. In contrast, under the condition of $H = 60$ km, $M = 20$, the strong viscous interaction leads to the evidently larger pressure than the corresponding inviscid pressure. In such conditions with strong viscous interaction, the local flow quantities captured by the Euler solver may have a large difference from those in a real flight condition, thus reducing the accuracy of LPT.

The 4% thickness circular-arc airfoil is used here to evaluate the capability of LPT. The forced oscillatory motion of the airfoil is described in the following equation:

$$\alpha = \alpha_0 + da \cdot \sin(\omega t) \quad (5)$$

In the test cases, $\alpha_0 = 0$ deg, $da = 1$ deg. The circular frequency ω is determined by a reduced frequency $k = \omega c / (2u_\infty) = 0.02$, where $c = 1$ m. The center of stiffness of all two-dimensional airfoil cases in this paper is chosen at the quarter-chord position without special instructions. Table 1 compares the amplitudes of unsteady

Table 1 Comparison of amplitudes of aerodynamic coefficients at different conditions

M	H , km	Re , m^{-1}	Amplitude					
			C_N (N-S) $\times 10^{-3}$	C_N (LPT) $\times 10^{-3}$	RE C_N , %	C_m (N-S) $\times 10^{-4}$	C_m (LPT) $\times 10^{-4}$	RE C_m , %
10	20	1.85×10^7	7.71	7.44	3.5	8.09	7.76	4.1
10	30	3.77×10^6	7.95	7.44	6.4	9.33	7.76	16.8
10	40	7.92×10^5	8.25	7.44	9.8	10.4	7.76	25.4
15	50	2.98×10^5	6.93	5.49	20.8	7.95	2.82	64.5

aerodynamic coefficients computed by unsteady N-S equations and LPT. A criterion is used in this paper that, for two-dimensional airfoils, if the relative error (RE) of amplitude is over 10% for C_N or over 20% for C_m , the approximate model is considered to be no longer applicable. We can find that the results of the two methods agree well for the cases with high Reynolds number, but the accuracy of the LPT method goes bad as the Reynolds number decreases. According to the criterion, LPT is no longer applicable at $H \geq 40$ km.

IV. Local Piston Theory with Viscous Correction

In hypersonic flow, the viscous interaction between the outer inviscid flow and the boundary layer is significant due to the very large boundary-layer thickness [2]. Because the flow outside the boundary layer can be considered as inviscid, we may obtain the effective shape of the object from the steady-state CFD N-S solutions and then use LPT with the local flow quantities along the effective shape to compute the unsteady aerodynamic loads. This method is called the local piston theory with viscous correction (VLPT).

A. Derivation of Local Piston Theory with Viscous Correction

The key to the method is the determination of a reasonable effective shape, which directly influences the accuracy of VLPT. There exists a corresponding relationship between vorticity and viscous flow. Specifically, for the boundary of viscous flow immediately adjacent to the surface, the flow is highly rotational with high vorticity. However, outside this boundary layer, the flow is generally lowly rotational with low or even zero vorticity [21]. As a result, vorticity can be taken as a characteristic quantity to distinguish the viscous flow inside the boundary layer from the inviscid flow outside the boundary layer, thus to determine the effective shape.

Vorticity is defined as

$$\xi = \nabla \times \mathbf{V} = \left(\frac{\partial w}{\partial y} - \frac{\partial v}{\partial z} \right) \mathbf{i} + \left(\frac{\partial u}{\partial z} - \frac{\partial w}{\partial x} \right) \mathbf{j} + \left(\frac{\partial v}{\partial x} - \frac{\partial u}{\partial y} \right) \mathbf{k} \quad (6)$$

For two-dimensional flows, only the third term is kept on the right side of Eq. (6). The laminar boundary-layer displacement thickness equation on a flat plate by Anderson for strong viscous interaction case [2,21] is

$$\delta^* \propto M^{1/2} Re^{-1/4} x^{3/4} \quad (7)$$

where Re is the unit Reynolds number, and x is the distance offset from a point in the body surface to the leading edge in the longitudinal section. From Eq. (6), we can see that vorticity depends only on the velocity derivatives of the flowfield. Assume that the normal gradient of the streamwise velocity is much larger than the gradient of the other directions, which is reasonable for most flows around the slender hypersonic configurations; we can get the following criterion to obtain the effective shape:

$$|\xi| < C_{\text{eff}} \frac{u_\infty}{M^{1/2} Re^{-1/4} x^{3/4}} \quad (8)$$

where C_{eff} is the effective shape determination coefficient and includes the possible factors that affect the effective shape. Based on the flowfield from the steady-state N-S solutions, the vorticity of each

mesh point is searched from the body surface to the outside flowfield along the normal direction. Then, at the position where the vorticity satisfies Eq. (8) first, the edge of the effective shape is determined and so are the local flow quantities.

The viscous interaction effect has a major influence on the displacement thickness of the boundary layer, and viscous interaction parameters denote the strength of the viscous interaction. Therefore, the effective shape determination coefficient C_{eff} may only depend on the viscous interaction parameter. Historically, several viscous interaction parameters were developed at different flight conditions for different kinds of aircraft. The parameter \bar{V}' is a widely used viscous interaction parameter derived from the Space Shuttle program [2]. Wilhite et al. [22] demonstrated the validity of \bar{V}' as a force coefficient correlation parameter under the strong viscous interaction condition ($0.005 < \bar{V}' < 0.08$), which is close to the cases studied here. Thus, the paper adopts \bar{V}' as the viscous interaction parameter, defined as

$$\bar{V}' = \frac{M\sqrt{C'}}{\sqrt{Re_L}} \quad (9)$$

where

$$C' = \frac{\rho' \mu'}{\rho_\infty \mu_\infty} \quad (10)$$

where ρ' and μ' are evaluated at the reference temperature T' within the boundary layer, and the reference length equals the chord length of the airfoil. A reference temperature method suggested by Anderson is employed here [21]

$$T' = 1.28 + 0.023M^2 + 0.58(T_w/T_\infty - 1) \quad (11)$$

The viscosity coefficient μ' is calculated by Sutherland's law:

$$\frac{\mu'}{\mu_0} = \left(\frac{T'}{T_0} \right)^{3/2} \frac{T_0 + 110.4}{T' + 110.4} \quad (12)$$

where $\mu_0 = 1.716 \times 10^{-5}$ kg/(m · s), and $T_0 = 273.11$ K. The wall temperature $T_w = 1000$ K is used for this paper. Through Eqs. (9–12), the viscous interaction parameter \bar{V}' can be determined at a given condition.

To find the relation between C_{eff} and \bar{V}' , a series of unsteady numerical simulations for the vibrating 4% thickness circular-arc airfoil are conducted at zero AOA with different \bar{V}' . Note that a laminar boundary layer, on which most strong viscous interaction theories are based, is assumed in the N-S calculations here because of the large Mach number and small Reynolds number. An isothermal wall condition with $T_w = 1000$ K is applied. And the paper adopts the perfect gas model, neglecting the real gas effect. For each case, vary C_{eff} until the amplitudes of unsteady aerodynamic coefficients from VLPT and unsteady CFD match best. The final results are listed in Table 2.

By observing and plotting the values of C_{eff} and \bar{V}' , a nearly linear relationship between C_{eff} and $\sqrt{\bar{V}'}$ is discovered, shown in Fig. 4. The expression for C_{eff} can be obtained through linear fitting:

Table 2 Conditions for C_{eff} determination

M	H , km	k	$\bar{V}' \times 10^{-2}$	C_{eff}	Amplitude					
					C_N (N-S) $\times 10^{-3}$	C_N (VLPT) $\times 10^{-3}$	RE C_N , %	C_m (N-S) $\times 10^{-4}$	C_m (VLPT) $\times 10^{-4}$	RE C_m , %
10	40	0.02	0.85	0.31	8.25	7.97	3.45	10.4	10.6	2.02
13	45	0.02	1.31	0.59	7.20	6.85	4.90	8.22	8.48	3.16
15	50	0.02	1.89	0.86	6.93	6.72	3.02	7.95	8.28	4.15
15	55	0.01	2.53	1.10	7.20	7.11	1.19	8.86	9.17	3.48
18	57	0.01	2.95	1.28	6.90	6.76	2.03	8.27	8.58	3.78
20	60	0.01	3.60	1.49	6.94	6.88	0.86	8.51	8.58	0.85

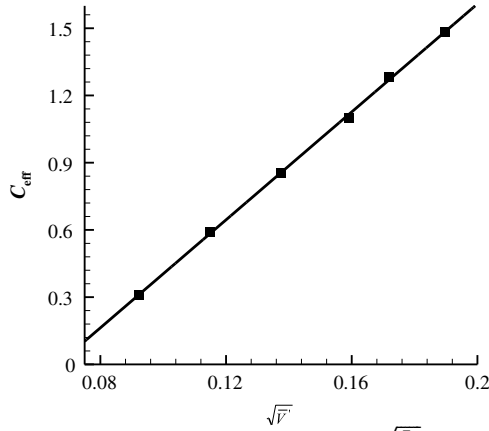


Fig. 4 Linear fitting of C_{eff} with $\sqrt{\bar{V}'}$.

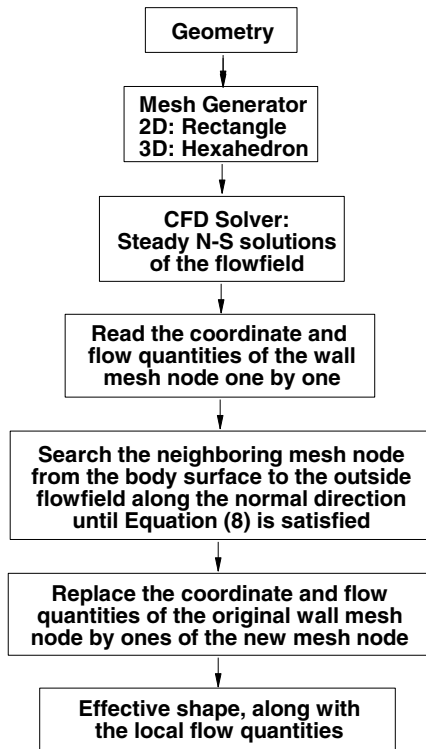


Fig. 5 Flowchart for obtaining the effective shape.

$$C_{\text{eff}} = 12.05 \sqrt{\bar{V}'} - 0.8 \quad (13)$$

Note that the coefficients may have a minor difference for different solvers or meshes, but the linear relationship should remain unchanged. A detailed process for obtaining the effective shape is summarized in Fig. 5.

B. Verification of Only Dependency on \bar{V}' for C_{eff}

To verify if there are other parameters that have a direct influence on C_{eff} , several cases considering different Mach number, altitude, unit Reynolds number, and chord length are conducted for the same

$\bar{V}' = 0.0189$. C_{eff} is equal to 0.856, calculated from Eq. (13). The results are listed in Table 3. We can see that using the same C_{eff} for the same viscous interaction parameter \bar{V}' is reasonable for different cases. Therefore, we infer that C_{eff} can be determined directly from \bar{V}' . In fact, the Mach number, altitude, and chord length are included in the expression of \bar{V}' , thus determining the value of C_{eff} indirectly.

C. Range of Application of Local Piston Theory with Viscous Correction

Based on the results from Table 2, the comparison of the amplitudes from VLPT and N-S is proceeded by increasing Mach number and altitude, listed in Table 4. For all cases, C_{eff} is calculated from Eq. (13). From the results, we can see that, at the altitude over 70 km, the VLPT method is no longer applicable according to the criterion set in Sec. III. A possible reason may be that, with further increase in Mach number and altitude, the thick boundary layer may merge with the shock wave: a merged shock layer. When this happens, the shock layer must be treated as fully viscous, and the conventional boundary-layer analysis must be completely abandoned [2]. Then, the concept of effective shape may not be valid anymore. Therefore, for a typical thin airfoil, a range of application for VLPT is suggested here: $0.0085 \leq \bar{V}' \leq 0.062$. Note that the lower limit corresponds to the condition where LPT is no longer applicable.

D. Variation of Effective Shapes

Effective shapes of the 4% thickness circular-arc airfoil are obtained at various flight conditions through the criterion in Eq. (8), depicted in Figs. 6–8. Several conclusions about the effective shape can be made. First, from Fig. 6, we can find that the effective shape turns a little thicker as the Mach number increases. However, the influence of the Mach number is so little as to be negligible. This is consistent with the Mach number independence principle: at high Mach numbers, the flowfield becomes essentially independent of Mach number [2]. Second, it is evident from Fig. 7 that increasing altitude makes the effective shape thicker. From the two preceding results, we see that the thickness of the effective shape varies consistently with the strength of the viscous interaction, namely, the effective shape turns thicker as the viscous interaction becomes stronger. Third, a predictable result, shown in Fig. 8, is that the lower surface of the effective shape becomes thinner and the upper surface becomes thicker with the increase in AOA.

V. Calculation of Unsteady Aerodynamic Loads

Several cases are conducted to evaluate the capability of VLPT. The unsteady aerodynamic characteristics of the 4% thickness circular-arc airfoil are calculated, from $\alpha_0 = 0$ to 20 deg, to test the validity of VLPT at large angles of attack. In addition, a set of circular-arc airfoils with different thickness are chosen to assess the effect of the airfoil thickness on the accuracy of VLPT. Finally, the case of an all-body model is conducted to evaluate the application of VLPT on three-dimensional problems. With all motions described by Eq. (5), amplitudes and time histories of the aerodynamic coefficients (including C_N and C_m) obtained from VLPT are compared with those obtained from the unsteady N-S equations and LPT. The unsteady N-S solutions are taken as the benchmark solutions.

For the two-dimensional airfoil cases, the chosen motion parameters are $da = 1$ deg, $k = 0.02$. The airfoils with 1 m length all pitch around its quarter-chord position. The base flight condition is $M = 15$ and $H = 50$ km.

Table 3 Different cases for the same \bar{V}'

M	H , km	$Re (\times 10^5)$, m^{-1}	c , m	Amplitude					
				C_N (N-S) $\times 10^{-3}$	C_N (VLPT) $\times 10^{-3}$	RE C_N , %	C_m (N-S) $\times 10^{-4}$	C_m (VLPT) $\times 10^{-4}$	RE C_m , %
9.7	40	7.68	0.2	8.94	9.31	4.14	12.50	13.30	6.40
13.7	45	5.25	0.5	7.24	7.31	0.97	8.66	9.26	6.93
15	50	2.98	1.0	6.93	6.72	3.02	7.95	8.28	4.15
15	55	1.67	1.8	6.93	6.52	5.92	7.97	8.08	1.38

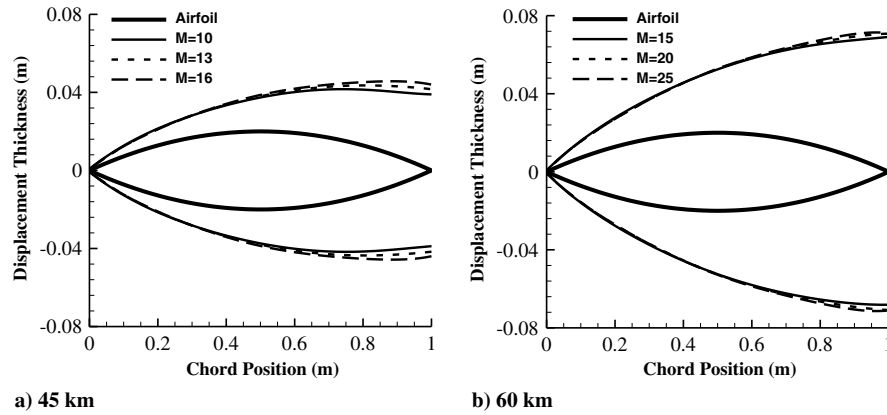
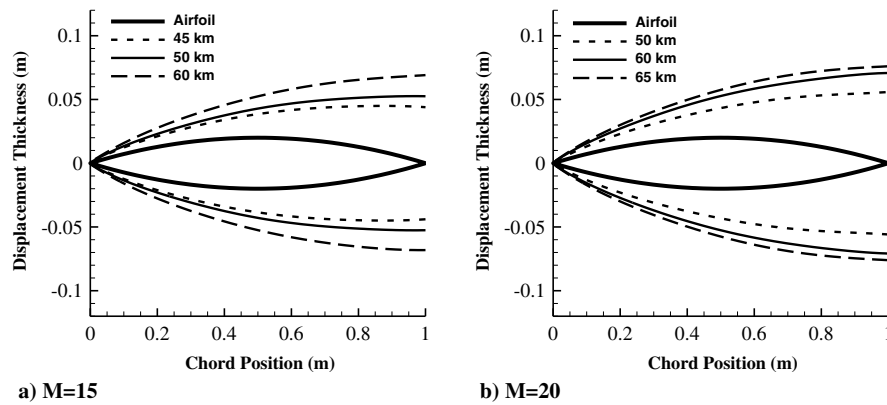
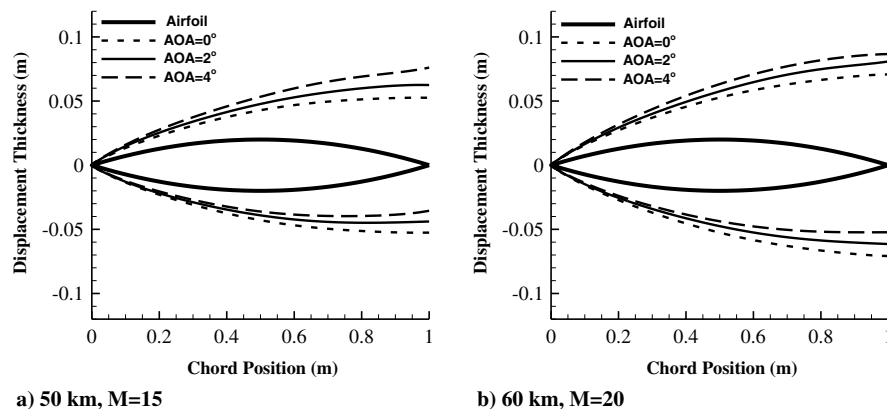
Table 4 Comparison of amplitudes at different cases ($k = 0.02$)

M	H , km	\bar{V}'	Amplitude					
			C_N (N-S) $\times 10^{-3}$	C_N (VLPT) $\times 10^{-3}$	RE C_N , %	C_m (N-S) $\times 10^{-4}$	C_m (VLPT) $\times 10^{-4}$	RE C_m , %
25	60	0.037	6.59	6.69	1.52	7.77	8.08	3.99
20	63	0.043	7.21	7.12	1.25	9.29	8.91	4.09
20	65	0.049	7.50	7.22	3.73	10.00	9.05	9.50
20	68	0.060	7.73	7.23	6.47	10.86	9.01	17.03
25	68	0.062	7.40	7.20	2.70	10.14	8.77	13.51
20	70	0.069	7.96	7.13	10.43	11.60	8.69	25.09
25	70	0.071	7.62	7.13	6.43	10.85	8.51	21.57

For the three-dimensional all-body cases, the motion parameters are: $d\alpha = 1^\circ$, $k = 0.0915$ (the reference length is 0.9144 m). The center of the pitching motion is set to be (0.54864 m, 0, 0). And the base flight condition is $M = 20$ and $H = 60$ km.

A. Effect of Angle of Attack

Figure 9 describes the time histories of unsteady aerodynamic coefficients at $\alpha_0 = 4^\circ$. Superior agreement between VLPT and N-S results is achieved. Note that the aerodynamic coefficients of

**Fig. 6** Comparison of effective shapes at different Mach numbers.**Fig. 7** Comparison of effective shapes at different altitudes.**Fig. 8** Comparison of effective shapes at different angles of attack.

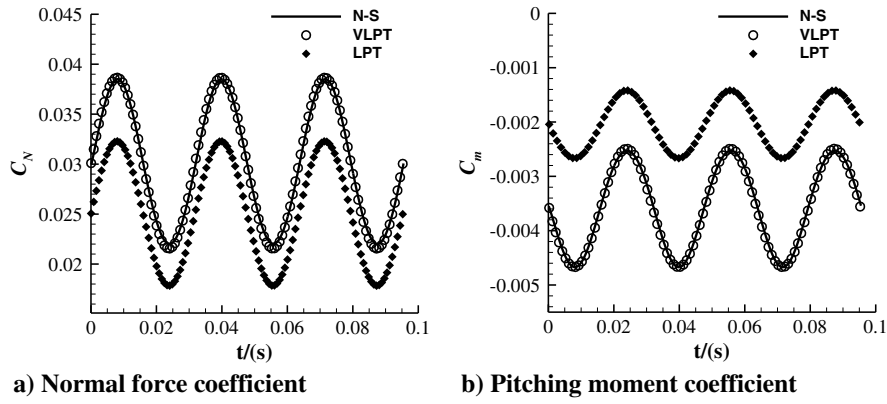


Fig. 9 Time histories of unsteady aerodynamic coefficients for the 4% circular-arc airfoil at $\alpha_0 = 4$ deg.

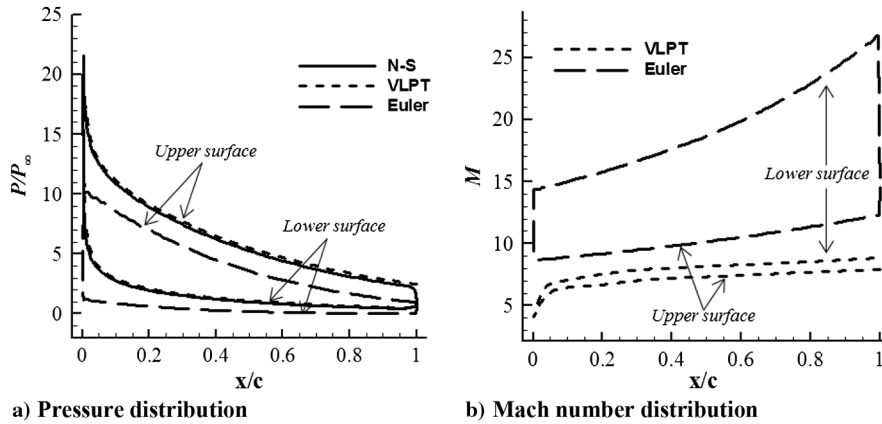


Fig. 10 Steady pressure and Mach number distribution for the 4% circular-arc airfoil at $\alpha_0 = 4$ deg.

VLPT are the integration on the effective shape, making the mean values slightly different from the steady N-S solutions that integrate on the original body surface. However, the steady N-S solutions are obtained before the application of VLPT. Hence, the mean values of VLPT can be corrected by the steady N-S solutions. Higher errors between LPT and N-S are shown in both mean values and amplitudes. The steady pressure and Mach number distributions at $\alpha_0 = 4$ deg from the three methods are depicted in Fig. 10. Compared to the results from the inviscid solution, the steady pressure on the effective shape is larger, and the Mach number is lower. Note that the Mach number on the original airfoil from the N-S solution is zero and not plotted in Fig. 10b. The combined influence of differences in the local flow quantities and the shape of the surface (the effective shape shown in Fig. 8a) lead to the deviations between the results from VLPT and LPT. In addition, the relative location of the pressure center along the chord is 33.5, 37.7, and 37.0% for the airfoil from the steady Euler solution, the effective shape, and original airfoil from the steady N-S solution, respectively, which makes the error of C_m appear relatively larger than that of C_N for LPT.

With the increase in AOA, disturbances relative to the freestream become larger, which may reduce the accuracy of VLPT and LPT. The amplitudes of unsteady aerodynamic coefficients for a set of angles of attack are shown in Fig. 11. Compared to N-S, the results of VLPT are good to excellent for a wide range of AOA. Specifically, the error of VLPT for C_N is lower than LPT at most angles of attack. The intersection of the two curves from LPT and N-S leads to the closer C_N by accident around $\alpha_0 = 12$ deg, which on the contrary shows that VLPT is more accurate than LPT in terms of the variation trend. For C_m , VLPT shows higher accuracy at all angles of attack. Although increasing the AOA makes the deviations higher between

VLPT and N-S, the maximum relative error is only 5% for C_N and 4.71% for C_m both at $\alpha_0 = 20$ deg, which is quite acceptable.

B. Effect of Airfoil Thickness

The airfoil thickness may have an influence on the accuracy of VLPT for two reasons. First, the boundary-layer displacement thickness formula in Eq. (7) is derived based on a flat plate, and thus the accuracy of the effective shape may be reduced for the airfoil with large thickness. Second, the accuracy of LPT may also be lowered as the thickness of airfoil increases [9] due to the larger streamwise perturbations. The amplitudes of unsteady aerodynamic coefficients for a series of circular-arc airfoils with different thickness, ranging from 4 to 16%, are plotted in Fig. 12. The variation trend for the amplitude of C_N is consistent for the three methods, whereas the error of LPT turns apparently larger than that of VLPT. The advantages of VLPT are expounded more significantly in the moment coefficients. A low accuracy of LPT is observed in both magnitude and variation trend. However, VLPT shows good agreement with N-S up to an airfoil thickness of 16%.

Furthermore, according to the criterion made in Sec. III, the applicable maximum AOAs for the circular-arc airfoils with different thickness are listed in Table 5. We can see that the airfoils with larger thickness have a lower applicable maximum AOA for VLPT. This is because increasing the thickness of airfoil itself exerts a larger compression angle of freestream, thus limiting the applicable range of AOA.

C. Application on an All-Body Model

The basic all-body model (without control surfaces) is a typical and relatively simple hypersonic lifting-body configuration derived

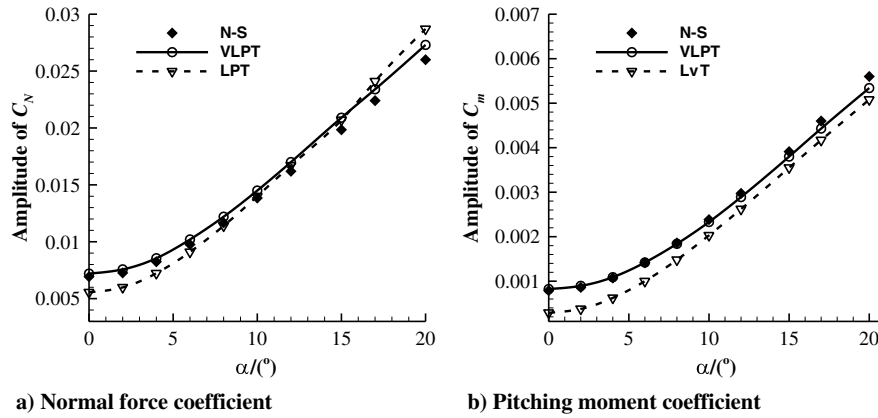


Fig. 11 Amplitudes of unsteady aerodynamic coefficients vs mean AOA for the 4% circular-arc airfoil.

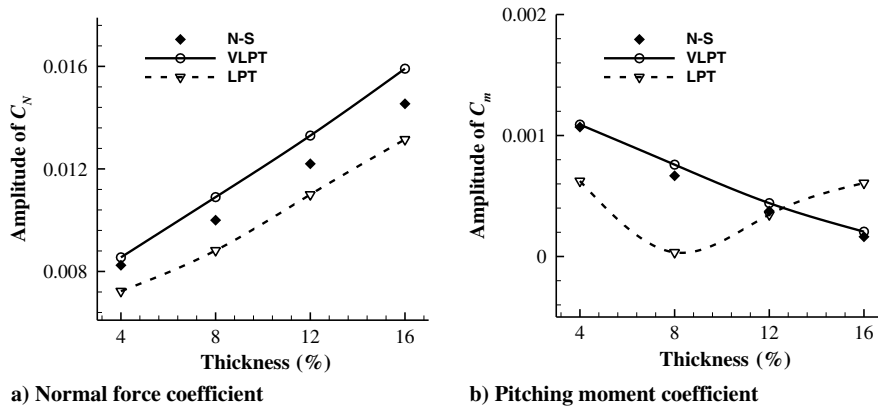


Fig. 12 Amplitudes of unsteady aerodynamic coefficients vs thickness for a set of circular-arc airfoils at $\alpha_0 = 4$ deg.

from analytical studies [23–25], shown in Fig. 13. The top-down view of the model is a triangle plane with a leading-edge sweepback of 75 deg. The total axial length is 0.9144 m. The model, including the forebody and afterbody, has elliptical cross sections. The major-to-minor axis ratio is 4 for the forebody. The height of the minor axis for the afterbody is continuously reduced backward up to a sharp straight-line trailing edge. The forebody and afterbody are connected at two-thirds of the body length.

The criterion for the determination of effective shape in Eq. (8) is derived from two-dimensional flows, and so the three-dimensional flow effects may reduce the accuracy of VLPT.

Figures 14 and 15 show the effective shape and pressure distribution of the longitudinal symmetric plane for the all-body at $\alpha_0 = 0$ deg, respectively. We can see that the effective shape is significantly thicker than the original body, which not only makes the pressure from the N-S and VLPT results larger than that from the Euler results but also alleviates the expansion of the flow on the rear half.

The time histories and amplitudes of the unsteady aerodynamic coefficients are shown in Figs. 16 and 17. The maximum relative error of VLPT is 12.31% for C_N and 28% for C_m both at $\alpha_0 = 10$ deg. However, the maximum relative error of LPT is 22.9% for C_N at $\alpha_0 = 0$ deg, and the errors for C_m are all unacceptably more than 53%. An evident improvement in accuracy is obtained by VLPT.

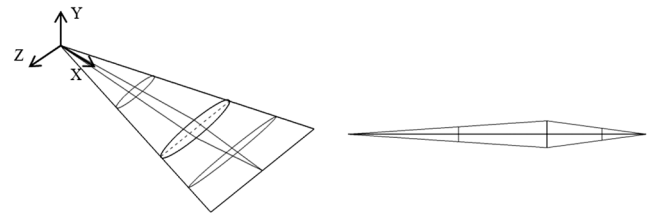


Fig. 13 All-body model.

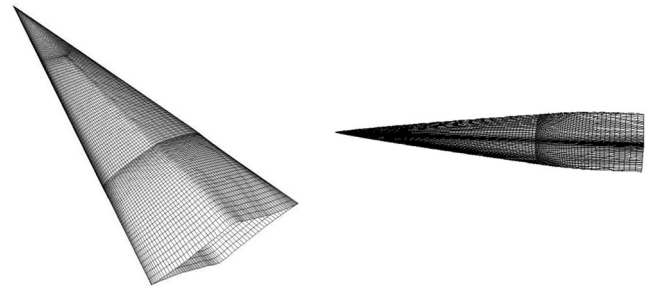


Fig. 14 Effective shape of the all-body model at $\alpha_0 = 0$ deg.

This demonstrates the validity of VLPT on the three-dimensional hypersonic configuration.

VI. Flutter and Dynamic Stability Analysis

The preceding sections have proved the feasibility and relatively high accuracy by employing the effective shape to correct the Euler-based local piston theory. In this section, the flutter predictions of a double-wedge airfoil and the pitching dynamic stability evaluations of a three-dimensional hypersonic waverider

Table 5 Maximum applicable AOA for circular-arc airfoils with different thickness for VLPT

Thickness, %	Maximum AOA, deg
4	≥ 20
8	≥ 20
12	15
16	9

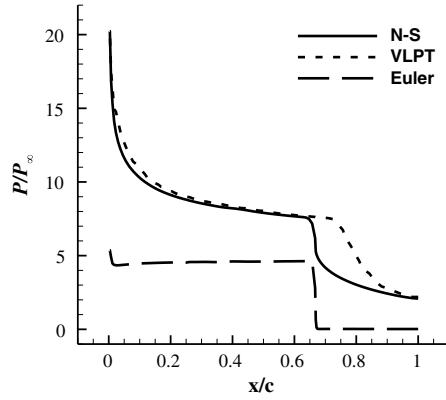


Fig. 15 Steady pressure distribution of the longitudinal symmetric plane of the all-body model at $\alpha_0 = 0$ deg.

configuration are operated under the condition of high altitudes and high Mach numbers to further assess the application and accuracy of VLPT.

A. Airfoil Flutter Predictions

According to Lagrange's equations, the two-degree-of-freedom linear system shown in Fig. 18 can be expressed in the following form:

$$\begin{cases} m\ddot{h} + S_\alpha\ddot{\alpha} + K_h h = -L \\ S_\alpha\ddot{h} + I_\alpha\ddot{\alpha} + K_\alpha \alpha = M_{EA} \end{cases} \quad (14)$$

Defining the dimensionless time $\tau_\omega = \omega_\alpha \cdot t$ and the generalized coordinates

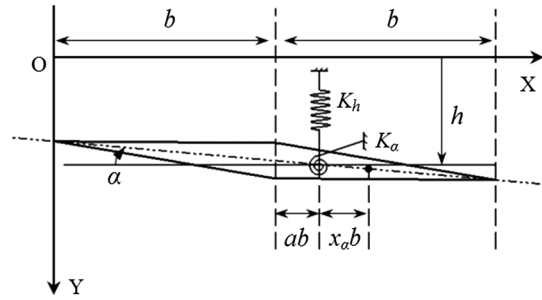


Fig. 18 Two-degree-of-freedom aeroelastic model of the airfoil.

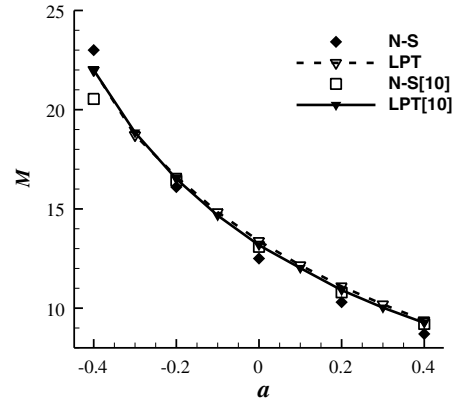
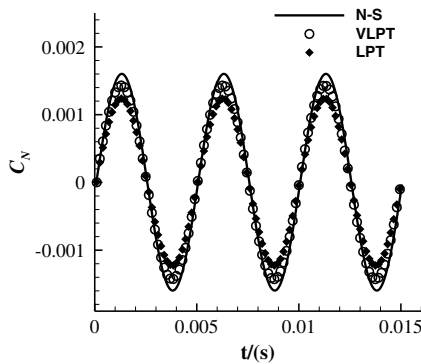
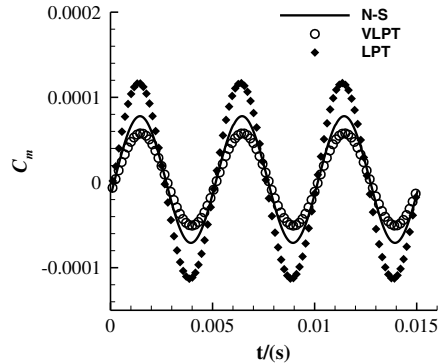


Fig. 19 Flutter Mach number vs elastic-axis offset parameter a , 40,000 ft.

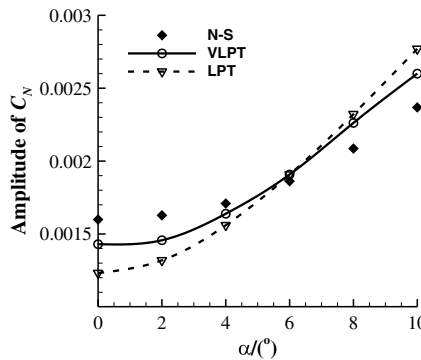


a) Normal force coefficient

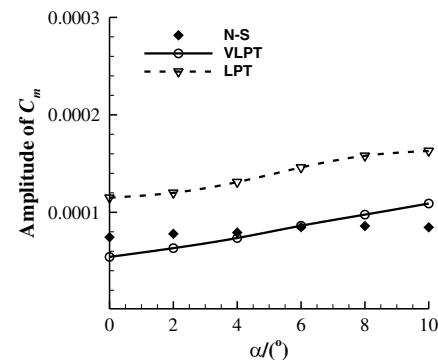


b) Pitching moment coefficient

Fig. 16 Time histories of unsteady aerodynamic coefficients for the all-body model at $\alpha_0 = 0$ deg.



a) Normal force coefficient



b) Pitching moment coefficient

Fig. 17 Amplitudes of unsteady aerodynamic coefficients vs mean AOA for the all-body model.

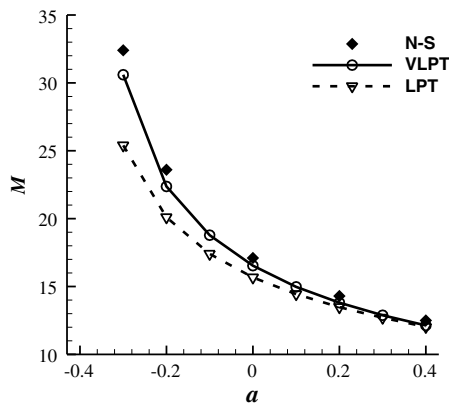
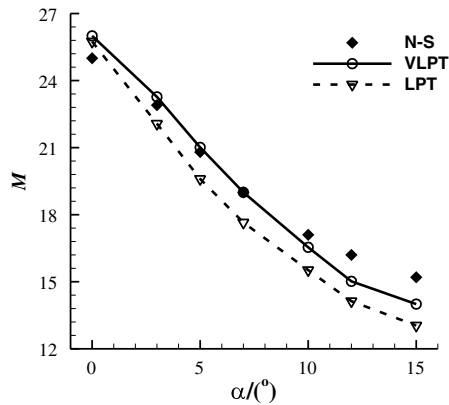
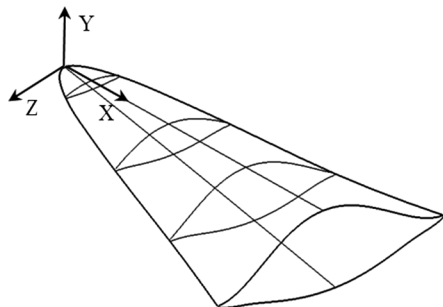
Table 6 Parameters describing the double-wedge airfoil [10]

Parameter	Value
c	2.35 m
τ	0.0336
m	94.2 kg/m
r_a	0.484
ω_a	37.6 Hz
ω_h/ω_a	0.3564
x_a	0.2

$$\zeta = \begin{Bmatrix} h/b \\ \alpha \end{Bmatrix}$$

we obtain

$$M\ddot{\zeta} + G\dot{\zeta} + K\zeta = F \quad (15)$$

**Fig. 20** Flutter Mach number vs elastic-axis offset parameter a , 40 km, $\alpha_0 = 10$ deg.**Fig. 21** Flutter Mach number vs AOA at $a = 0$, 40 km.**Fig. 22** Waverider model.

where

$$M = \begin{bmatrix} 1 & x_a \\ x_a & r_a^2 \end{bmatrix}, \quad G = 0, \quad K = \begin{bmatrix} (\omega_h/\omega_a)^2 & 0 \\ 0 & r_a^2 \end{bmatrix},$$

$$F = \frac{\rho u_\infty^2}{m \omega_a^2} \begin{Bmatrix} -C_l \\ 2C_m \end{Bmatrix}$$

In [10], flutter boundaries of a double-wedge airfoil, described in Table 6, are predicted with several aerodynamic models at 40,000 and 60,000 ft. Note that VLPT cannot be applied in such altitudes even if the Mach number is very high. For example, under the condition of $H = 60,000$ ft and $M = 30$, the viscous interaction parameter \bar{V}' is very small ($1.26e-3$), and a negative C_{eff} (-0.373) is obtained according to Eq. (13). The criterion in Eq. (8) is no longer valid. Therefore, the effective shape cannot be acquired at such low altitudes by the methodology proposed in this paper.

To verify the accuracy of the current aeroelastic codes, the flutter Mach numbers of the double-wedge at 40,000 ft are predicted by the current solver GMFlow, LPT, and corresponding results from [10], shown in Fig. 19. Excellent agreements are obtained between

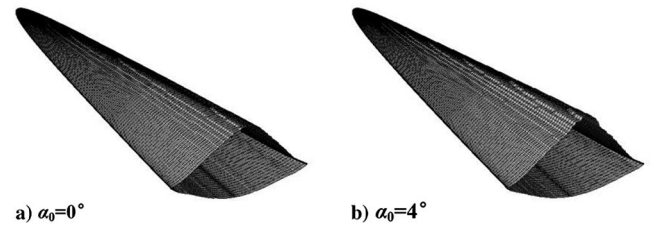
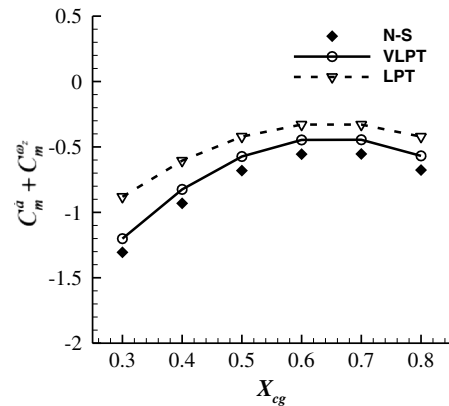
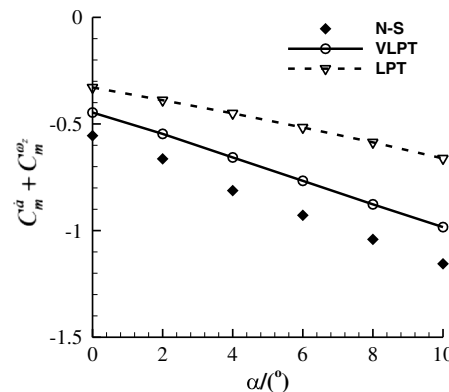
**Fig. 23** Effective shapes of waverider, at $H = 55$ km, $M = 15$.**Fig. 24** Damping-in-pitch derivative vs the relative position of center of gravity at $\alpha_0 = 0$ deg.**Fig. 25** Damping-in-pitch derivative vs AOA at $X_{cg} = 0.6$.

Table 7 Viscous interaction parameter at different conditions

H , km	M	$\bar{V}' (\times 10^{-3})$
10	45	5.48
15	50	8.45
15	55	11.3
20	60	16.1
20	65	22.1

different N-S or different LPT results, which demonstrates that the current solver is credible in the application of aeroelasticity. In addition, the flutter boundaries predicted by LPT are rather close to those by N-S, showing that, in such conditions even with very high Mach numbers, the viscous interaction effect is not strong enough to affect the flutter boundaries significantly, and the use of LPT is sufficient to obtain satisfying flutter results.

To verify the application of VLPT on aeroelasticity, the altitude of 40 km is chosen to perform the flutter predictions. Note that the flutter Mach numbers should be no more than 30 so that the condition $M\tau < 1.0$ for piston theory is satisfied. At 40 km, if the same parameters of the double-wedge airfoil were used, the flutter Mach numbers would be much higher than 30 due to the very low air density. Therefore, a lower torsional stiffness, $\omega_\alpha = 7.96$ Hz, is used here, with the other parameters listed in Table 6 kept unchanged.

The flutter Mach numbers at different elastic-axis offset positions, ranging from -0.3 to 0.4 , at $\alpha_0 = 10$ deg are shown in Fig. 20. With the N-S results taken as the benchmark solution, it can be seen that the error of LPT increases as a decreases, and the maximum relative error is 21.62% at $a = -0.3$. Nevertheless, the error of VLPT is evidently lower than that of LPT, especially at the position $a \leq 0$. The maximum error of VLPT is simply 5.56% at $a = -0.3$. Furthermore, flutter boundaries at different angles of attack are predicted by the three different methods, shown in Fig. 21. Apparently, a better agreement with the N-S results is achieved by VLPT. The preceding results demonstrate that, under the condition of strong viscous interaction, VLPT is able to predict more accurate flutter boundaries than LPT, which may also indicate that the effect of viscosity on the aeroelastic behavior could be captured using effective shape corrections.

B. Damping-in-Pitch Derivative Calculations of a Waverider

An accurate evaluation of the damping-in-pitch derivative is important for the design of any hypersonic aircraft in that it plays an important role in the decay of the amplitude of AOA and represents the single freedom pitching dynamic stability characteristic. Here, we employ a widely used method [26], based on the forced oscillation technique, to evaluate the damping-in-pitch derivative, calculated as follows:

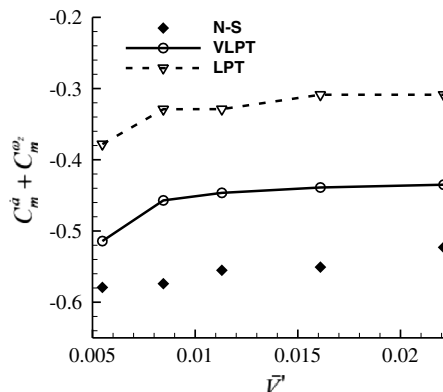


Fig. 26 Damping-in-pitch derivative vs viscous interaction parameter at $X_{cg} = 0.6$ and $\alpha_0 = 0$ deg.

$$C_m^{\omega_z} + C_m^{\dot{\alpha}} = \frac{1}{\pi \alpha} \int_{-\pi}^{\pi} C_m \cos(k\tau) d\tau \quad (16)$$

A detailed derivation is given in Appendix A. We can see that an accurate calculation of unsteady pitching moment is the key to the evaluation of the damping-in-pitch derivative.

A typical hypersonic cone-derived waverider configuration is studied here, shown in Fig. 22 (described in Appendix B). The effective shapes are shown in Fig. 23. Note that the positive pitching moment corresponding to the nose-up moment is ruled here. The center of gravity along the Y axis is -0.15 m, and the origin of coordinates is located at the nose of the waverider. At the flight condition of $H = 55$ km and $M = 15$, the damping-in-pitch derivatives as a function of the center of gravity and AOA are shown in Figs. 24 and 25, respectively. The two approximate models both underestimate the pitching dynamic stability at all centers of gravity and angles of attack, whereas VLPT exhibits evidently higher accuracy than LPT. Furthermore, a set of viscous interaction parameters are chosen, listed in Table 7, to assess the damping-in-pitch derivative. The results are shown in Fig. 26. Likewise, VLPT agrees better with N-S results, with the maximum relative error being only 20%, which is acceptable for the calculation of damping-in-pitch derivative. Comparing the results obtained from LPT and VLPT, we can conclude that the viscous interaction has a stabilizing effect on the pitching dynamic characteristics for the waverider configuration.

VII. Conclusions

The accuracy of Euler-based local piston theory is greatly reduced at high altitudes and large Mach numbers due to the strong inviscid-viscous interactions. This paper introduces a method to determine the effective shape through a relationship between vorticity and the viscous interaction parameter, based on the laminar boundary-layer displacement thickness formula and the solution of steady N-S equations. Then, a local piston theory with viscous correction is developed by using the effective shape.

It is found that the effective shape becomes thicker with the increase in the strength of the viscous interaction. The influence of large airfoil thickness and large AOA on the accuracy of VLPT is investigated by two-dimensional circular-arc airfoil cases. A high accuracy is obtained by VLPT up to the airfoil with a thickness of 16%. It is also found that the applicable maximum AOA lowers as the airfoil thickness increases. Compared with LPT, significant improvement in accuracy is also achieved by VLPT for a three-dimensional all-body model. Furthermore, VLPT is applied for the flutter boundary predictions of a double-wedge airfoil and the pitching dynamic stability evaluations of a three-dimensional hypersonic waverider configuration. The flutter Mach numbers obtained by VLPT show good agreement with those by the unsteady N-S equations, whereas large deviations emerge for LPT as a result of the strong viscous interaction effect. Results suggest that the effect of viscosity on the aeroelastic behavior could be captured using effective shape corrections. Likewise, the damping-in-pitch derivative calculated by VLPT is close to that by the unsteady N-S equations. We also find that the viscous interaction effect acts in a stabilizing manner for the pitching dynamic characteristics.

In summary, the results show that the proposed VLPT is an effective tool to efficiently and accurately evaluate the unsteady aerodynamic characteristics of hypersonic aircraft in the preliminary design phase.

Appendix A: Derivation of the Damping-in-Pitch Derivative

The forced pitching oscillation is described in a dimensionless form of Eq. (5):

$$\alpha = \alpha_0 + d\alpha \cdot \sin(k_c \tau_c) \quad (A1)$$

where

$$k_c = \frac{\omega c}{u_\infty}, \quad \tau_c = \frac{t}{c/u_\infty}$$

According to the Etkin model [27], for a harmonic motion, the pitching moment coefficient can be written as

$$C_m = C_m(\alpha, \dot{\alpha}, \ddot{\alpha}, \dots, \omega_z, \dot{\omega}_z, \ddot{\omega}_z, \dots) \quad (\text{A2})$$

For hypersonic problems, only the linear items need to be kept as a result of the weak time-history effect. Therefore, based on Taylor series expansion, we have

$$C_m = C_{m_0} + C_m^\alpha \Delta\alpha + C_m^{\omega_z} \Delta\omega_z + C_m^{\dot{\alpha}} \Delta\dot{\alpha} + C_m^{\dot{\omega}_z} \Delta\dot{\omega}_z \quad (\text{A3})$$

for the pitching forced oscillation motion, $\Delta\alpha = \Delta\dot{\omega}_z$, combined with Eq. (A1), we obtain

$$C_m = C_{m_0} + (C_m^\alpha - k_c^2 C_m^{\dot{\omega}_z}) d\alpha \cdot \sin(k_c \tau_c) + (C_m^{\omega_z} + C_m^{\dot{\alpha}}) k_c d\alpha \cdot \cos(k_c \tau_c) \quad (\text{A4})$$

C_m can be expanded as the following form of Fourier series:

$$C_m = \frac{1}{2\pi} \int_{-\pi}^{\pi} C_m d(k_c \tau_c) + \frac{1}{\pi} \int_{-\pi}^{\pi} C_m \sin(k_c \tau_c) d(k_c \tau_c) \cdot \sin(k_c \tau_c) + \frac{1}{\pi} \int_{-\pi}^{\pi} C_m \cos(k_c \tau_c) d(k_c \tau_c) \cdot \cos(k_c \tau_c) \quad (\text{A5})$$

Compare the third term of the right side of Eqs. (A4) and (A5); we can obtain the following expression of the damping-in-pitch derivative:

$$C_m^{\omega_z} + C_m^{\dot{\alpha}} = \frac{1}{\pi d\alpha} \int_{-\pi}^{\pi} C_m \cos(k_c \tau_c) d\tau_c \quad (\text{A6})$$

Appendix B: Generation of the Waverider

The detailed introduction of the cone-derived waverider can be seen in [28]. Given a basic flowfield of a cone, the shape of the waverider can be determined through a base curve on the base surface, shown in Fig. B1. The basic curve is described with the following fourth-order polynomials:

$$Y = -(b_0 + b_2 Z^2 + b_4 Z^4) \quad (\text{B1})$$

Define a parameter $k_{wr} = R_0/R_s$, and choose a boundary condition where the slope is zero at the points the base curve intersects the shock curve in the base surface [29]; then, the coefficients in the preceding equation can be determined as

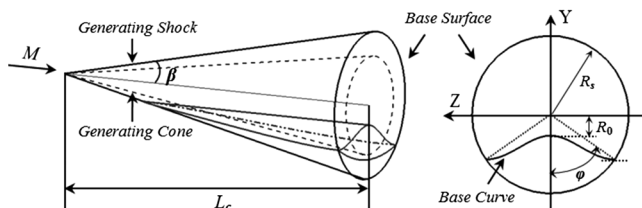


Fig. B1 Generation of waverider.

Table B1 Basic condition and geometric parameters used to define the waverider

M	β	k_{wr}	φ	L_c
15	12 deg	0.5	40 deg	1 m

$$\begin{cases} b_0 = k_{wr} L_c \tan \beta \\ b_2 = \left(\frac{\cos \varphi}{k_{wr}} - 1 \right) \cdot \frac{2b_0}{L_c^2 \tan^2 \beta \sin^2 \varphi} \\ b_4 = -\frac{b_2}{2L_c^2 \tan^2 \beta \sin^2 \varphi} \end{cases} \quad (\text{B2})$$

The basic flow condition and relevant parameters are listed in Table B1. The created waverider is scaled up to 5 m length. Finally, a radius of 10 mm is blunted along the leading edge. The blunting method proposed in [30] is employed.

Acknowledgments

The work was supported by the National Natural Science Foundation of China (91216205 and 11272319) and carried out at the National Supercomputer Center in Tianjin, and the calculations were performed on TianHe-1(A). The authors would also like to thank Bao-Fang Song from the Center of Applied Space Technology and Microgravity at the University of Bremen for his suggestions of writing.

References

- [1] Guruswamy, G. P., "Unsteady Aerodynamic and Aeroelastic Calculations for Wings Using Euler Equations," *AIAA Journal*, Vol. 28, No. 3, March 1990, pp. 461–469. doi:10.2514/3.10415
- [2] Anderson, J. D., Jr., *Hypersonic and High-Temperature Gas Dynamics*, 2nd ed., AIAA, Reston, VA, 2006.
- [3] Anderson, J. D., Jr., *Modern Compressible Flow with Historical Perspective*, 3rd ed., McGraw-Hill, New York, 2003.
- [4] Lighthill, M. J., "Oscillating Airfoils at High Mach Numbers," *Journal of the Aeronautical Sciences*, Vol. 20, No. 6, June 1953, pp. 402–406. doi:10.2514/8.2657
- [5] Van Dyke, M., "A Study of Second-Order Supersonic Flow Theory," NACA TR 1081, 1951.
- [6] Morgan, H. G., Runyan, H. L., and Huckel, V., "Theoretical Considerations of Flutter at High Mach Numbers," *Journal of the Aeronautical Sciences*, Vol. 25, No. 6, June 1958, pp. 371–381.
- [7] Scott, R. C., and Pototzky, A. S., "Quasisteady Aerodynamics for Flutter Analysis Using Steady Computational Fluid Dynamics Calculations," *Journal of Aircraft*, Vol. 33, No. 1, Jan.–Feb. 1996, pp. 191–197. doi:10.2514/3.46921
- [8] Zhang, W. W., "Efficient Analysis for Aeroelasticity Based on Computational Fluid Dynamics," Ph.D. Dissertation, Northwestern Polytechnical Univ., Xi'an, PRC, 2006 (in Chinese).
- [9] Zhang, W. W., Ye, Z. Y., Zhang, C. A., and Liu, F., "Supersonic Flutter Analysis Based on Local Piston Theory," *AIAA Journal*, Vol. 47, No. 10, Oct. 2009, pp. 2321–2328. doi:10.2514/1.37750
- [10] McNamara, J. J., Crowell, A. R., Friedmann, P. P., Glaz, B., and Gogulapati, A., "Approximate Modeling of Unsteady Aerodynamics for Hypersonic Aeroelasticity," *Journal of Aircraft*, Vol. 47, No. 6, Nov.–Dec. 2010, pp. 1932–1945. doi:10.2514/1.C000190
- [11] McNamara, J. J., and Friedmann, P. P., "Aeroelastic and Aerothermoelastic Analysis in Hypersonic Flow: Past, Present, and Future," *AIAA Journal*, Vol. 49, No. 6, June 2011, pp. 1089–1122. doi:10.2514/1.J050882
- [12] Cox, R. N., and Crabtree, L. F., *Elements of Hypersonic Aerodynamics*, English Univ. Press, London, 1965.
- [13] Han, H. Q., Zhang, C. A., and Wang, F. M., "An Approximate Model of Unsteady Aerodynamics for Hypersonic Problems at High Altitude," *Chinese Journal of Theoretical and Applied Mechanics*, Vol. 45, No. 5, Sept. 2013, pp. 690–698 (in Chinese). doi:10.6052/0459-1879-12-382

- [14] Boer, A., Schoot, M. S., and Faculty, H. B., "Mesh Deformation Based on Radial Basis Function Interpolation," *Computers and Structures*, Vol. 85, Nos. 11–14, March 2007, pp. 784–795.
doi:10.1016/j.compstruc.2007.01.013
- [15] Jiang, Y. W., "Numerical Solution of Navier–Stokes Equations on Generalized Mesh and Its Application," Ph.D. Dissertation, Northwestern Polytechnical Univ., Xi'an, PRC, 2012 (in Chinese).
- [16] Hua, R. H., Zhao, C. X., Ye, Z. Y., and Jiang, Y. W., "Effect of Elastic Deformation on the Trajectory of Aerial Separation," *Aerospace Science and Technology*, Vol. 45, April 2015, pp. 128–139.
doi:10.1016/j.ast.2015.04.015
- [17] Kou, J. Q., and Zhang, W. W., "An Approach to Enhance the Generalization Capability of Nonlinear Aerodynamic Reduced-Order Models," *Aerospace Science and Technology*, Vol. 49, Feb. 2016, pp. 197–208.
doi:10.1016/j.ast.2015.12.006
- [18] Landon, R. H., "NACA0012 Oscillatory and Transient Pitching," AGARD Rept. 702, Dataset 3, Neuilly sur Seine, France, 1982.
- [19] "Aerodynamic Design Data Book, Volume 1: Orbital Vehicle," NASA CR-160386, 1978.
- [20] Zhang, W. W., Shi, A. M., Wang, G., and Ye, Z. Y., "On Determining Unsteady Aerodynamic Loads Accurately and Efficiently," *Journal of Northwestern Polytechnical University*, Vol. 22, No. 5, Oct. 2004, pp. 545–549 (in Chinese).
doi:1000-2758(2004)05-0545-05
- [21] Anderson, J. D., Jr., *Fundamentals of Aerodynamics*, 4th ed., McGraw–Hill, New York, 2005.
- [22] Wilhite, A. W., Arrington, J. P., and McCandless, R. S., "Performance Aerodynamics of Aero-Assisted Orbital Transfer Vehicles," *22nd Aerospace Sciences Meeting*, AIAA Paper 1984-0406, Jan. 1984.
- [23] Gregory, T. J., Wilcox, D. E., and Williams, L. J., "The Effects of Propulsion System-Airframe Interactions on the Performance of Hypersonic Aircraft," *3rd Propulsion Joint Specialist Conference*, AIAA Paper 1967-0493, July 1967.
- [24] Gregory, T. J., Williams, L. J., and Wilcox, D. E., "The Airbreathing Launch Vehicle for Earth Orbit Shuttle—Performance and Operation," *Advanced Space Transportation Meeting*, AIAA Paper 1970-0270, Feb. 1970.
- [25] Lockman, W. K., Lawrence, L. L., and Cleary, J. W., "Flow over an All-Body Hypersonic Aircraft: Experiment and Computation," *Journal of Spacecraft and Rockets*, Vol. 29, No. 1, Jan.–Feb. 1992, pp. 7–15.
doi:10.2514/3.26308
- [26] "Dynamic Stability Parameters," AGARD CP-235, Neuilly sur Seine, France, Nov. 1978.
- [27] Etkin, B., *Dynamics of Atmospheric Flight*, Wiley, New York, 1972, pp. 158–159.
- [28] Jones, M. J., Moore, M. K., Pike, M. J., and Roe, M. J., "A Method for Designing Lifting Configurations for High Supersonic Speeds Using Axisymmetric Flow Fields," *Ingenieur-Archiv*, Vol. 37, No. 1, Jan. 1968, pp. 56–72.
doi:10.1007/BF00532683
- [29] Chen, X. Q., Hou, Z. X., and Liu, J. X., "Orthogonality Experiment Analysis of Conical and Osculating-Cone Waverider," *47th AIAA Aerospace Sciences Meeting*, AIAA Paper 2009-1466, Jan. 2009.
- [30] Tincher, D. J., and Burnett, D. W., "A Hypersonic Waverider Flight Test Vehicle: The Logical Next Step," *30th Aerospace Sciences Meeting and Exhibit*, AIAA Paper 1992-0308, Jan. 1992.

M. Smith
Associate Editor